

# Active Image-based Modeling

Rui Huang, Danping Zou, Richard Vaughan, Ping Tan

**Abstract**—We seek to automate the data capturing process in image-based modeling, which is often tedious and time consuming now. At the heart of our system is an iterative linear method to solve the multi-view stereo (MVS) problem quickly. Unlike conventional MVS algorithms that solve a per-pixel depth at each input image, we represent the depth map at each image as a piecewise planar triangle mesh and solve it by an iterative linear method. The edges of the triangle mesh are snapped to image edges to better capture scene structures. Our fast MVS algorithm enables online model reconstruction and quality assessment to determine the next-best-views (NBVs) for modeling. The NBVs are searched in a plane above unreconstructed shapes. In this way, our path planning can use the result from 3D reconstruction to guarantee obstacle avoidance. We test this system with an unmanned aerial vehicle (UAV) in a simulator, an indoor motion capture system (Vicon) room, and outdoor open spaces.

## I. INTRODUCTION

Image-based modeling techniques create 3D models from digital images. These methods often follow a standard pipeline of structure-from-motion (SfM) [1][2][3], multi-view stereo (MVS) [4], and surface modeling and texturing [5][6]. The SfM step calibrates all cameras and reconstructs a sparse set of 3D point cloud. The MVS step computes a much denser point cloud, e.g. a 3D point per pixel, to facilitate the surface modeling. The surface modeling and texturing step generates the final triangle mesh of the scene and creates texture maps for visualization purposes. This modeling pipeline has been extensively studied in the field of computer vision and computer graphics [7][8][9]. It has been demonstrated at different scales including desktop objects, statues and buildings, and cities [4][10]. Now, both open source [11] and commercial softwares [12][13] are available to reconstruct high quality 3D model from images.

Almost all existing image-based-modeling methods take a fixed set of images as input, where the 3D modeling pipeline has no influence on image acquisition. In practice, the input images are often insufficient to reconstruct the 3D model due to motion blur, undersampling, or occlusion. Under these unfavorable conditions, the user will have to re-capture additional images to cover the missing part while maintaining sufficient view overlap with the original data. The user often needs to conduct an on-site survey and experiment with several iterations of image capturing and modeling to get a satisfactory result. The data capturing process is often tedious, time consuming, and difficult especially for novice users.

We present an active image-based modeling method to automate image capture. Our system puts image capturing in the optimization loop in order to actively plan the flight of an autonomous UAV to guarantee good image coverage.

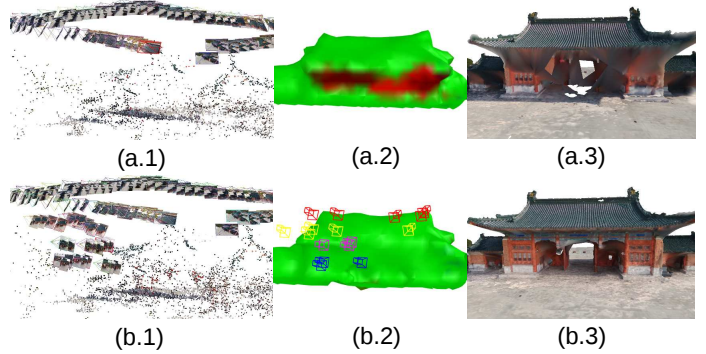


Fig. 1: Modeling of an Asian building after the initial data capturing (a) and actively capturing more data (b). The figures (a.1), (b.1) show the SfM point clouds and camera poses, (a.2), (b.2) are color-coded model quality evaluation, where red indicates poor results, (a.3), (b.3) are the final 3D models generated from those images.

Our system achieves this goal by: 1) efficiently solving the image-based modeling problem; 2) assessing the model quality to select additional views; and 3) planning additional flight paths while avoiding potential obstacles. Fig. 1 shows an Asian building modeled by our system. After an initial flight, the image-based modeling result has large errors in concave regions under the roof as shown in (a.2) and (a.3). Our system can actively capture more images to cover those regions as demonstrated in (b.2) and (b.3). The camera positions and orientations can also be seen from the SfM results in (a.1) and (b.1) respectively.

We make several contributions to make this system possible. Firstly, we propose a novel MVS algorithm that is much faster than conventional MVS algorithms, e.g. our method can reconstruct 100 images in about 20 seconds whereas conventional methods need hours on the same inputs. Our rapid MVS algorithm enables online active image-based modeling for the first time. Secondly, we propose a novel next-best-view (NBV) algorithm that is tailored to fit our modeling method. Our NBV algorithm is designed to facilitate obstacle avoidance. At the same time, it balances two competing factors: 1) maintaining view overlap with captured images and 2) covering missing regions of the object. It ensures complete coverage and smooth transition between neighboring images so that 3D reconstruction can proceed.

Our complete system has been tested in simulation, indoors with Vicon, and open outdoor space. Experimental results show effectiveness and efficiency of our active 3D modeling system.

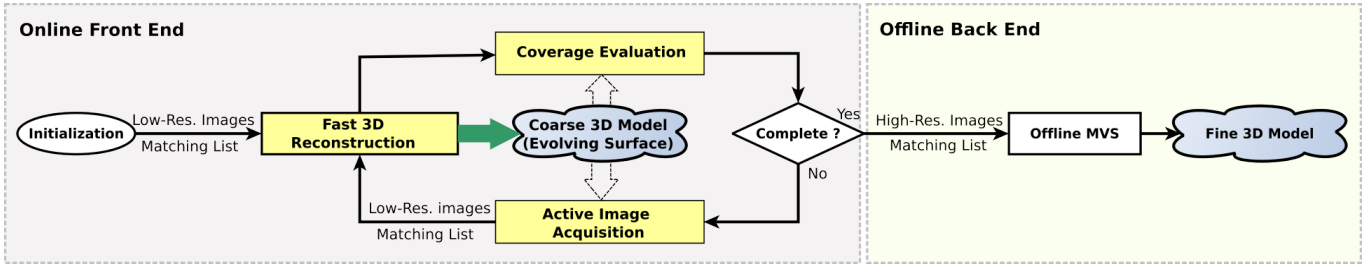


Fig. 2: Our system consists of an online front end and an offline back end. The front end captures images automatically to ensure good coverage of the object. The back end takes an existing method [10] to build a high quality 3D model.

## II. RELATED WORK

*a) Multiple-View Stereo (MVS):* MVS aims to compute a per-pixel 3D point for each input image. Classic MVS algorithms are often based on volumetric graph-cut [14, 15], level-set optimization [16], or iteratively matching-propagation [17, 18]. Due to the heavy optimization task, MVS is the most time consuming process in the image-based modeling pipeline, and usually takes hours to reconstruct a scene at the scale of our examples. The high computational complexity prevents its usage in online processing. It is recently shown that dense piecewise planar surfaces can be reconstructed from a single view from sparse SfM points [19]. This method is fast as it only involves solving a linear equation. Our MVS algorithm is inspired by this work, but our method is not limited to a single image and works well on multiple views.

*b) Next-Best-View (NBV) Planning:* The NBV problem is a classic problem in robotics [20, 21] to identify a set of views for producing a complete and precise 3D model. It is a hard problem because the actual 3D shape of the scene is unknown, thus it is difficult to precisely determine the NBV. Many NBV methods [22, 23, 24] are heuristic, relying on holes, open boundaries, or point densities to find NBVs. These methods work well in relatively simple scenes. They cannot deal with complex scenes like an urban area, because the local open boundaries are often far different from actual missing part, leading to bad view selections. A recent method [25] first does a Poisson surface reconstruction to obtain a best guess of the 3D shape, and then searches for NBVs accordingly.

Another difficulty of the NBV problem is the large search space. Typically, the solution space is quantized into a 3D voxel grid [25, 22], and each candidate position needs to be evaluated to identify the NBVs. Some methods [26, 27] restrict the solution space to a sphere surface to reduce computation at the cost of reducing the chance of finding the true NBVs. Other methods [28] only consider candidate viewpoints with a constant distance to the object to deal with large scale objects.

We also use Poisson surface reconstruction to build a rough 3D model for NBV planning. The reconstruction also helps our UAV avoid obstacles.

*c) Active 3D Modeling System:* Active 3D modeling systems put data acquisition in the loop of modeling, producing partial results that guide further data acquisition. This problem has been studied with depth sensors [25, 22, 23] on small

scale objects. Generalizing this idea to color cameras and to architecture scale scenes is much harder. Hoppe et al. [29] have demonstrated such a system with conventional (and time-consuming) MVS algorithm [17], where the NBVs are selected by the covariance of the mesh vertices. Due to the poor efficiency of MVS, their system is not demonstrated for online processing, which limits its application on complicated scenes requiring multiple iterations of data capturing. In comparison, Mostegel et al. [30] use machine learning techniques to predict the MVS quality without actually executing it. In this way, they can also infer NBVs to improve the final MVS result.

Our system is unique in the following aspects. Firstly, we design a fast MVS algorithm to obtain a dense reconstruction quickly. This enables us to exploit the Poisson surface reconstruction to evaluate the model quality, which is typically limited to depth sensor or offline methods. This improvement on model accuracy leads to better NBV planning and more efficient image capturing allowing our system to handle more complex scenes. Secondly, thanks to our high quality MVS result, we can search NBVs in a plane above all uncertain shapes to ensure obstacle avoidance. We also introduce *virtual update* for view candidate evaluation to sample many NBVs at once, which helps to improve efficiency in dealing with large scale scenes.

## III. OVERVIEW

Our system consists of an online front end and an offline back end as shown in Fig. 2. The front end controls the image capturing process to ensure good data coverage. The back end takes an existing method [10] to build a high quality 3D model from the captured images. We focus on the front end that consists of mainly three components: *Fast 3D Modeling*, *Coverage Evaluation*, and *Active Image Acquisition*. The *Fast 3D Modeling* component uses down-sampled images to quickly generate a coarse 3D model. The *Coverage Evaluation* component assesses the completeness of the current 3D model and identifies those places that require additional images. When more images are needed, the *Active Image Acquisition* component determines a sparse set of camera views that are of the best chance to improve the 3D model and plans a flight path to drive the UAV to those positions. The path planning here takes the coarse 3D model into consideration to avoid possible collisions on the way. The UAV's position is provided by GPS or Vicon in our outdoor and indoor experiments

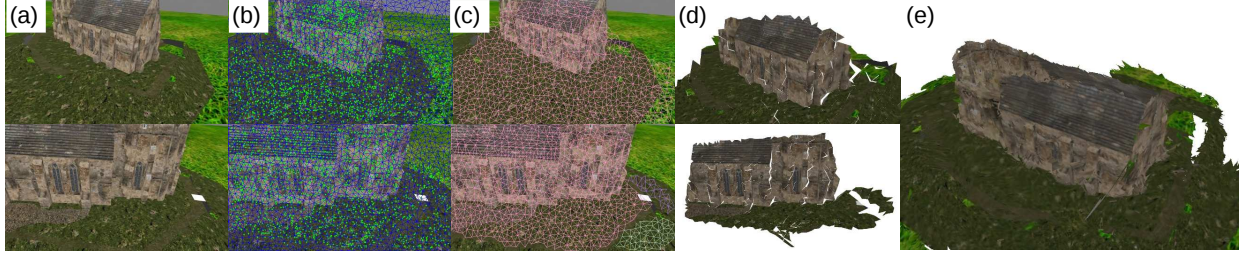


Fig. 3: Our novel linear piecewise planar MVS: (a) Input images; (b) 2D Delaunay triangulation; (c) Connected regions; (d) Mesh reconstructed from single view; (e) The mesh after multi-view depth fusion.

respectively. In the following sections, we will present details of each component.

#### IV. METHOD

##### A. Fast 3D Modeling

As shown in Fig. 2, the *Fast 3D Modeling* is called in the loop of online process whenever more images are captured. Its efficiency is therefore critical to make the front end fast. Here, we propose a novel method to solve a dense reconstruction efficiently. The basic idea is to use the sparse points from SfM as seeds, and image textures as cues, to solve a depth map in the form of a triangular mesh at each input image. Though this method produces coarser results comparing with conventional MVS, it is sufficient for the following *Coverage Evaluation*.

1) *Sparse Reconstruction*: We take a standard incremental SfM method [31] to calibrate all cameras and reconstruct a sparse set of 3D scene points. For better efficiency, we only match nearby images whose GPS positions are within 2 meters. When additional images are captured, the model is updated incrementally rather than recomputed from scratch.

2) *Linear Dense Surface Reconstruction*: Traditional MVS algorithms solve a per-pixel depth for each input image. To speedup this process, we regularize the depth map to a piecewise linear surface. This idea is exemplified in Fig. 3. Specifically, as shown in Fig. 3 (a-b), we divide each input image into polygons by an over-segmentation algorithm [32]. Each polygon is split into triangles via the Delaunay triangulation [33]. These triangles are further clustered into connected regions covering SfM points as in Fig. 3 (c). Instead of solving a per-pixel depth for each image, we solve a per-vertex depth for each triangle, which is formulated as a linear equation and fast to solve. This produces a 3D triangle mesh for each input image as shown in Fig. 3 (d). We further require the triangle meshes from different views to agree with each other by enforcing the multi-view constraint. Therefore, the results from different views can be naturally fused as in Fig. 3 (e).

Consider a triangle  $\{v_1, v_2, v_3\}$ . We seek to compute the depth at  $v_1, v_2$  and  $v_3$ . Suppose  $p$  is a point reconstructed by SfM, and  $p$  is projected in the triangle  $\{v_1, v_2, v_3\}$ . The inverse depth of  $p$  can be interpolated from inverse depths of three vertices:

$$d_p = \alpha_1 d_1 + \alpha_2 d_2 + \alpha_3 d_3. \quad (1)$$

Here,  $d_p$  and  $d_k$  are the inverse depths of  $p$  and  $v_k, 1 \leq k \leq 3$  respectively. The weights  $(\alpha_1, \alpha_2, \alpha_3)$  are the barycentric coordinates of  $p$  in the triangle  $\{v_1, v_2, v_3\}$ . We define an energy

$$E_{sfm}(i) = (d_p - \alpha_1 d_1 - \alpha_2 d_2 - \alpha_3 d_3)^2, \quad (2)$$

and minimize it to enforce consistency with SfM points. Here,  $i$  is the index for the input image.

Now, consider two adjacent triangles, instead of using classic triangle mesh representation as shown in Fig. 5 (a), we solve the depth for each individual triangle. As shown in Fig. 5(b),  $\{v_1, v_2, v_3\}$  and  $\{v_4, v_5, v_6\}$  are two neighboring triangles. Although  $v_3$  and  $v_5$  ( $v_2$  and  $v_6$ ) overlap in the image, we parameterize them with two distinctive depths, because the edge  $v_2 v_3$  might be an occluding edge and the two triangles are at different depths. We enforce local continuity that stitches the two edges  $v_2 v_3$  and  $v_5 v_6$  together. This continuity term is defined as

$$E_{continuity}(i) = w_c((d_3 - d_5)^2 + (d_2 - d_6)^2). \quad (3)$$

Here, the weight  $w_c$  controls the smoothness strength, which is determined by the color difference of the triangles.

At the same time, we encourage neighboring triangles to be coplanar, where the inverse depth of  $v_4$  can be computed by

$$d_4 = \beta_1 d_1 + \beta_2 d_2 + \beta_3 d_3, \quad (4)$$

where  $\{\beta_1, \beta_2, \beta_3\}$  are the barycentric coordinates of  $v_4$  with respect to the triangle  $\{v_1, v_2, v_3\}$ . To enforce coplanarity at neighboring triangles, we minimize a smoothness energy,

$$E_{smooth}(i) = w_c(d_4 - \beta_1 d_1 - \beta_2 d_2 - \beta_3 d_3)^2. \quad (5)$$

Now, we consider two neighboring views  $i, j$  as shown in Fig. 5 (c). We hope the triangle meshes solved at different views are consistent with each other. Suppose the triangle  $\{v'_1, v'_2, v'_3\}$  in the  $j$ -th view is projected to cover the vertex  $v_1$  in the  $i$ -th view. We denote their inverse depth as  $d'_1, d'_2$  and  $d'_3$  respectively. Then the depth at  $v_1$  should be consistent with the one interpolated from  $d'_1, d'_2$  and  $d'_3$  according to the barycentric coordinates. In other words, we should minimize the following energy,

$$E_{fusion}(i, j) = (d_1 - \gamma_1 d'_1 - \gamma_2 d'_2 - \gamma_3 d'_3)^2 \quad (6)$$

where  $(\gamma_1, \gamma_2, \gamma_3)$  are the barycentric coordinates of the  $v_1$  in the projected triangle  $\{v'_1, v'_2, v'_3\}$ . We typically consider a



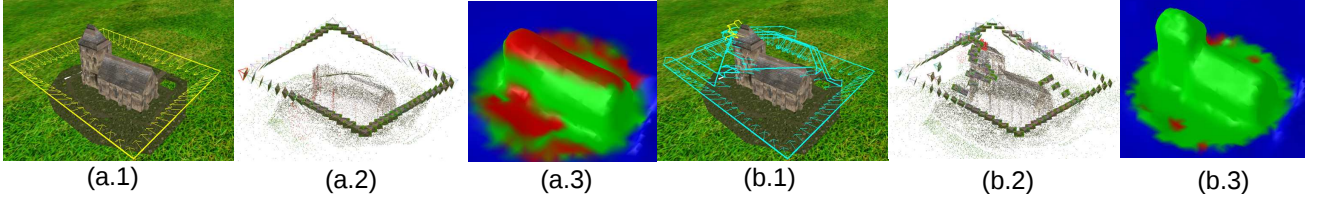


Fig. 4: The *Church* example. We show the results after the first and last iteration of image capture in (a) and (b) respectively. (a.1) and (b.1) are visualization of the flight paths. (a.2) and (b.2) are the SfM results (including sparse 3D points and camera poses), (a.3) and (b.3) are the coverage result, with uncovered (red) and covered (green) regions.

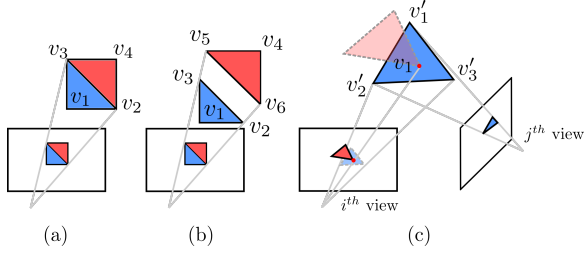


Fig. 5: Neighboring triangles are forced to have  $C^0$  continuity with the parameterization in (a), while the parameterization in (b) (splitting  $v_2, v_3$  in (a) to two vertices) allows discontinuity. Triangles are projected to neighboring views to enforce multi-view consistency as in (c).

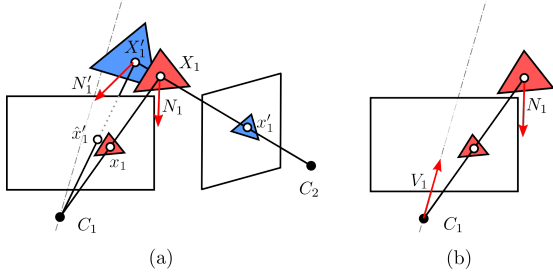


Fig. 6: Confidence evaluation based on cues from position/normal consistency (a) and the front parallelism.

fixed number of neighboring views (e.g. 6 neighbors in our experiments) to build this constraint.

Putting all together, we can write the energy function as

$$E = \sum_i E_{sfm}(i) + \sum_i E_{continuity}(i) + \sum_i E_{smooth}(i) + \sum_{|i-j|<3} E_{fusion}(i, j). \quad (7)$$

Note that except the fusion term, all other terms are linear functions of the vertex depths. The fusion term is nonlinear, because the inverse depth of  $v'_k, 1 \leq k \leq 3$  in the  $i$ -th view is not a linear function of its depth in the  $j$ -th view.

3) *Optimization Details*: To solve Eq. (7), we take an iterative linear approach, and first solve a depth map at each input image respectively by ignoring the fusion term. Later, we enforce the fusion term to improve the depth maps.

a) *Initialization*: This step simply discards the fusion term  $E_{fusion}$  and minimizes the remaining terms per each

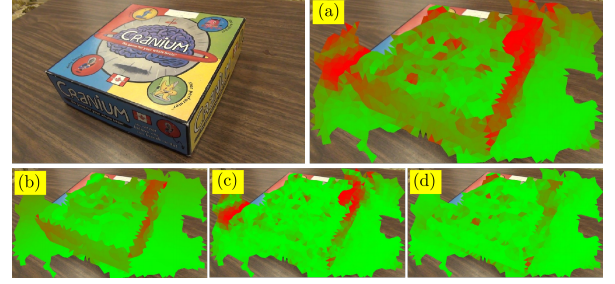


Fig. 7: An input image and its depth confidence map (a), which is computed according to confidences scores from position consistency (b), surface normal consistency (c) and front parallelism (d).

view by solving a linear equation. In this way, the original energy function becomes a linear function,

$$\|\mathbf{d}_{sfm} - \mathbf{A}\mathbf{d}\|^2 + \lambda_s \|\mathbf{B}\mathbf{d}\|_{\mathbf{W}_s}^2 + \lambda_c \|\mathbf{C}\mathbf{d}\|_{\mathbf{W}_c}^2 + \lambda_u \|\mathbf{d}_{ref} - \mathbf{R}\mathbf{d}_L\|^2. \quad (8)$$

Here  $\mathbf{d}_{sfm}$  is a  $N_s \times 1$  vector representing the inverse depths of all SfM points and  $\mathbf{d}$  is a  $N_v \times 1$  vector of unknown inverse depth of all mesh vertices.  $\mathbf{A}$  is a  $N_s \times N_v$  sparse matrix where each row contains the barycentric coordinates as in Eq. (2).  $\mathbf{B}$  is a sparse matrix collecting all the smoothness constraints as described in Eq. (5). Each row of  $\mathbf{C}$  consists of only 1 and -1 to describe the continuity constraint defined in Eq. (3). Both  $\mathbf{W}_s$  and  $\mathbf{W}_c$  are diagonal matrices consisting of color difference penalty  $w_c$  between adjacent triangles.  $\mathbf{R}$  and  $\mathbf{d}_{ref}$  are both derived from Eq. (6), which respectively represents an identity matrix and depths of the corresponding triangles.  $\lambda_s, \lambda_c$  and  $\lambda_u$  are weights of each constraint. Eq. (8) can be efficiently minimized by a linear solver.

b) *Confidence*: The initialization step can generate large errors, especially at occlusion edges. We fuse results from other views to help reduce errors. To facilitate fusion, we compute a confidence score at each triangle to measure its quality derived from three cues: position consistency, normal consistency, and front parallelism.

*Position Consistency*: Suppose a triangle is reconstructed from the  $i$ -th view and its centroid  $X_1$  is projected at  $x_1$  as shown in Fig. 6(a). To ensure the consistency, we project  $X_1$  to a neighboring view  $j$  at  $x'_1$  and find the corresponding 3D position  $X'_1$  from the  $j$ -th depth map. Let  $\hat{x}'_1$  be the projection of  $X'_1$  on the  $i$ -th image. The smaller distance between  $x_1$  and  $\hat{x}'_1$ , i.e.  $e_p = \|x_1 - \hat{x}'_1\|$ , indicates better consistency.

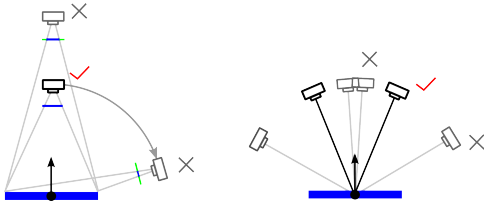


Fig. 8: Coverage evaluation on an iso-point. **Left:** Large projection ratio indicates that a view is well posed with respect to the iso-point - it is captured from nearby front parallel viewpoint. **Right:** A well-posed stereo configuration is a pair of views whose principal axes form an angle within a reasonable range. A too large angle could confuse feature matching, and a too small one will lead to a large depth uncertainty.

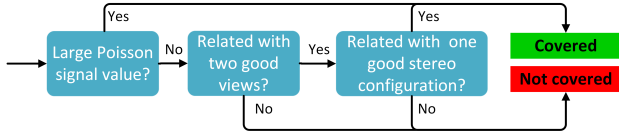


Fig. 9: Logical flow of classification of an iso-point being covered or not.

**Normal Consistency:** As shown in Fig. 6(a), let  $N_1$  be the normal direction of the triangle reconstructed from the  $i$ -th view and  $N_1'$  be the normal direction of corresponding triangle from the  $j$ -th view. We simply check the consistency by measuring the difference between these two normal directions, i.e.  $e_n = \arccos(N_1^T N_1')$ .

**Front Parallelism:** Generally speaking, when the viewing directions of camera are perpendicular to the object surface, SfM algorithms tend to produce more reliable 3D points. From this observation, we additionally measure the angle between the principal axis of the  $i$ -th camera and the estimated face normal  $N_1$ , i.e.  $e_v = \arccos(N_1^T V_1)$  to evaluate the reconstruction quality.

For each triangle, we evaluate the above confidence measurements with respect to  $N_{adj}$  neighboring views. We take the mean position consistency  $\bar{e}_p$  and normal consistency  $\bar{e}_n$  of  $N_{adj}$  views and define the overall confidence measurement as

$$\Gamma = \exp(-\bar{e}_p/\sigma_p) \exp(-\bar{e}_n/\sigma_n) (1 - \exp(-\cos^2(e_v)/\sigma_v)) \quad (9)$$

where constants  $\sigma_p, \sigma_n$  and  $\sigma_v$  control the weight of each confidence measurement. Fig. 7 illustrates the confidence map of a surface.

**c) Fusion:** Once a confidence map is computed for each view, we start to fuse the depth maps by solving Eq. (7). We still solve the depth map at one view at a time. Consider a triangular face  $f$  reconstructed from view  $i$ . If its confidence score is higher than 0.5, we leave its vertex fixed in Eq. (7). Otherwise, we optimize its depth by registering it to the corresponding triangles in other views by minimizing Eq. (7). We also exclude corresponding triangles too far away in 3D

space or with very different colors.

## B. Coverage Evaluation

Coverage evaluation aims to identify poorly reconstructed triangles to facilitate the next-best-view selection and flight path planning. We apply Poisson surface reconstruction [34] to the reconstructed triangle vertices. Poisson reconstruction generates a smooth surface with signals to indicate the density of vertices. We firstly crop the Poisson reconstructed mesh by a sphere of interest to exclude irrelevant regions. We further simplify the mesh by edge collapse to make the following computation faster. After that we uniformly sample the mesh by Poisson disk sampling [6] to get sampled points named as *iso-points*. We then evaluate model completeness at each iso-point by the following steps.

**a) Poisson Signal Assessment:** The first cue is the signal value returned by Poisson surface reconstruction. Signal value describes local density of the original point clouds. A region with high signal value indicates that it is well reconstructed as more points have been obtained, while the region with low signal value usually lacks of textures or camera coverage. Therefore, we mark those iso-points with signal value (from the closest vertex in original Poisson mesh) higher than  $s_{min} = 7$  as ‘covered’.

**b) Resolution Assessment:** Next, we further evaluate iso-points with low signal values. Intuitively, a surface is better reconstructed when it has higher resolution in the image. Here we define a *projection ratio* to measure the effective resolution of a vertex. Let  $A_p$  be the area of a small disk at an *iso-point*  $p$  in the 3D space and  $a_p(v)$  be the area of its projection on the image as shown in Fig. 8. *Projection ratio* of this iso-point is defined as  $\gamma_p(v) = a_p(v)/A_p$ . As shown in Fig. 8(a), a large projection ratio means the surface has high resolution in the image and better chance of high quality reconstruction. Therefore, for each iso-point, we mark views that lead to a projection ratio larger than a threshold  $\gamma_{min}$  as *well-posed*. If an iso-point has less than two well-posed views, it is marked as ‘uncovered’.

**c) Stereo Configuration Assessment:** For iso-points with at least two well-posed views, we further check the angle between the rays connecting the iso-point and the camera centers as shown in Fig. 8(b). If the angle is within a proper range  $[\theta_{min} = 2^\circ, \theta_{max} = 30^\circ]$ , the camera views form a good stereo configuration and the point is marked as ‘covered’. Otherwise, the point is marked as ‘uncovered’.

Fig. 9 shows the classification pipeline of ‘covered’ and ‘uncovered’ iso-points. Fig. 10 shows a coverage map. From left to right, those are the reconstructed triangle vertices by our fast MVS method, a 3D model by the offline MVS method [10], the evaluated coverage map, where ‘covered’ and ‘uncovered’ points are shown in green and red respectively. We can see that the 3D model in the middle have poor quality at ‘uncovered’ red regions shown in the right.

## C. Active Image Acquisition

In the following, we present our Next-Best-View (NBV) algorithm to determine additional viewpoints and path planning



Fig. 10: An example of the coverage map. Left: reconstructed points from our MVS; middle: 3D model from the offline back end modeling method [10]; right: a color coded coverage map, evaluated on the Poisson reconstructed surface.

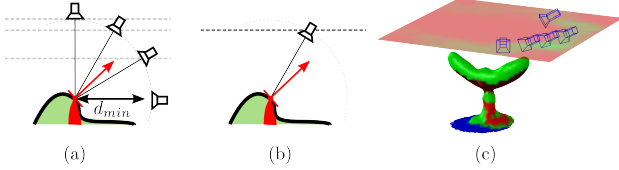


Fig. 11: Searching NBVs. Some ‘uncovered’ iso-point are marked in red. (a) For each quantized pitch angle, we determine a altitude according to the pitch angle and a minimum safe distance. (b) We choose the pitch angle (and its associated altitude) by the one that generates the NBV candidate with highest score. (c) Some local maximums are selected as the NBVs on the plane.

method to drive the UAV to the target positions and capture more images with proper orientation.

1) *Next-Best-Views (NBV)*: It is known that the NBV problem is NP-hard [21][25] and is often solved approximately by greedy algorithms. The computational complexity comes from the solution space quantization and candidate view evaluation. In principle, we need to discretize a 5D space (pitch, yaw and x,y,z coordinates) to search for NBVs. Though there are recent NBV algorithms for small desktop objects with a laser scanner [22][23], these methods are still too computational expensive for our large-scale outdoor scenes.

Our NBV planning method is designed for better efficiency and to guarantee obstacle avoidance. We first quantize the camera pitch angle into a few discrete values. We uniformly sample 12 pitch angles between  $[-30^\circ, 30^\circ]$ . For any sampled pitch angle  $\theta_p$ , we ignore iso-points whose normal directions pointing away ( $> 60^\circ$ ) from  $\theta_p$ , because they are barely visible from the chosen pitch angle  $\theta_p$ . We then select the highest remaining iso-point and determine a desired altitude of the UAV. The altitude is chosen such that the highest ‘uncovered’ point is projected to the image center, according to  $\theta_p$  and a predetermined minimum safe distance between obstacles and the UAV, as shown in Fig. 11. This altitude defines a plane

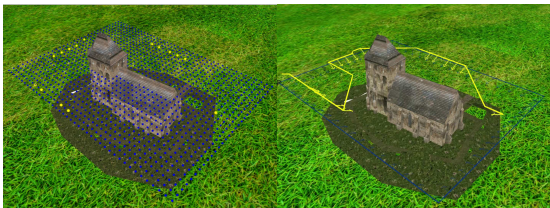


Fig. 12: Left: NBVs found on a plane; Right: Planned flight path by the A\* algorithm.

$H_\theta$  the UAV should fly in, which is above un-reconstructed regions.

Now, for any pitch angle  $\theta_p$  we have fixed the UAV at a particular altitude. We then search in the plane  $H_\theta$  for some NBVs. We uniformly sample a 2D grid of viewpoints in the plane  $H_\theta$  and uniformly sample 8 yaw angles for each viewpoint. A good NBV should capture as many ‘uncovered’ iso-points as possible and be well posed with respect to those ‘uncovered’ points at the same time. Therefore, we use the sum of *projection ratio* of those ‘uncovered’ iso-points as a score to evaluate a candidate. On each plane  $H_\theta$ , we select  $N_{nbv}$  ( $= 5$  in our experiments) local maximums as our NBVs with non-maximum suppression with radius of 1 meter. We further exclude candidates that are too far away from existing views to ensure successful feature matching in SfM. By too far, we mean the pitch and yaw angles differ by more than  $15^\circ$  or the position differ by more than 0.5 meters in indoor (or 3 meters in outdoor) experiments. Finally, among the 12 sampled pitch angles, we chose the one (and its associated altitude) that can bring the NBV with highest score.

In principle, provided the 5 selected NBVs we should let the UAV to take images at those viewpoints, update the model, and re-evaluate to identify the NBVs for the next iteration. However, to reduce the computation in 3D modeling, we decide to take more NBVs, e.g. 15 NBVs instead of 5. But we cannot simply take 15 local maximums in the score map, because the first 5 NBVs might make the others not a NBV. So we propose a *virtual update* of the coverage evaluation once some NBVs are selected. To compute a virtual update of the coverage evaluation, we ignore the *Poisson Signal Assessment* and compute the *Resolution Assessment* and *Stereo Configuration Assessment*, since the later two do not require actual images to evaluate. In this way, we always generate 15 NBVs in an iteration.

2) *Path Planning*: After NBVs have been obtained, we plan a path starting from the current position to all NBVs. To avoid collision, we generate an occupancy map on the plane where NBVs are found. We first discretize the plane into regular cells, mark those cells whose distance to the reconstructed 3D model is smaller than the safe distance as ‘occupied’ and mark the other cells as ‘free’. The distance from each cell to the 3D mesh is computed efficiently by the axis-aligned bounding boxes (AABB) tree [35] which stores the mesh for fast intersection and distance queries. A-star algorithm is used to generate a obstacle-free path connecting the NBVs starting from the current UAV position. When the UAV arrives at an NBV, it adjusts its yaw angle and camera pitch to take an image. Then it moves to the nearest NBV. The UAV captures both low resolution and high resolution images at each NBV position. Low resolution images are used for online fast 3D modeling, while high resolution images are used for offline MVS to build the final 3D model.

## V. EXPERIMENTS

We verify our system with both simulated and real experiments. For simulation, we use the Gazebo simulation





Fig. 13: NBV selection at the first four iterations. Notice that the drone gradually lower its altitude and tilt upward its camera to capture the missing region under the wings.

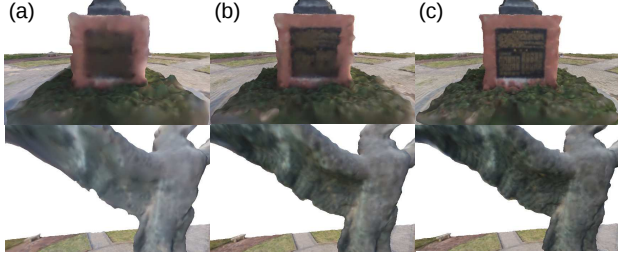


Fig. 14: (a). The *Eagle* example. (b-d). High resolution models by CMP-MVS after the 1st, 4th, and 8th iteration.

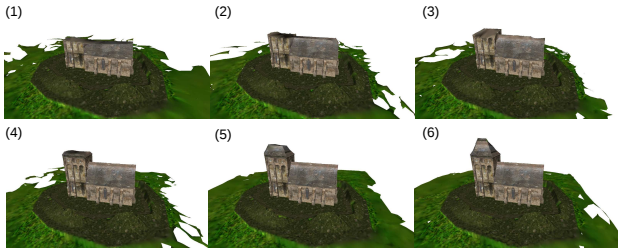


Fig. 15: High resolution models produced offline from CMP-MVS after each iteration.

platform [36] and 3D architecture models from 3D Warehouse [37]. For real experiments, we tested in both indoor Vicon rooms and outdoor open fields with a Bebop drone, where the UAV's localization is achieved by Vicon and GPS respectively. The Bebop drone sent images back via a WiFi link, and all computations are done on a Asus GL552 laptop with i7-CPU and 16 GB RAM. We present results in the following sections. More intermediate results can be found in the supplementary file.

#### A. Simulated Experiments

1) *Church*: As shown in Fig. 4 (a.1), the UAV takes images at some initial viewpoints sampled along a simple rectangular path over the object of interest. The camera's initial pitch angle is  $30^\circ$  downward. Fig. 4 (a.2) shows the results from SfM with 64 low-res ( $640 \times 368$ ) images at the initial positions, and (a.3) shows the coverage evaluation result. From these images, a 3D model can be generated by the offline CMP-MVS method [10] as shown in Fig. 15 (1). It is clear that 'uncovered' vertices correspond to poor final 3D modeling, e.g. the missing roofes. This *Church* example is fully covered in 6 iterations of image capturing. Fig. 4 (b.1) shows the additional flight paths and sampled viewpoints. The 3D positions and orientations of these views can be seen in (b.2). The coverage result in (b.3) suggests the model is well-constrained by these images.

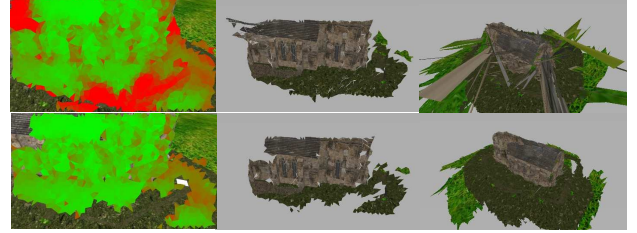


Fig. 16: Triangle depth map estimation. The first and second rows are results before and after multiview fusion. From left to right, they are: (a) confidence measure of the depth map, where red means low confidence; (b) sample depth map from a single view. (c) fused depth map from all views.

System Module	Running time (s)
Over-segmentation	6.9
Delaunay Triangulation	0.6
Our MVS – Initialization	1.4
Our MVS – Confidence	1.0
Our MVS – Fusion	4.5
Poisson Surface Reconstruction	20.0
NBV Selection	6.1
Path Planning	< 0.01

TABLE I: System running time

This can be verified in Fig. 15, which shows a 3D modeling by CMP-MVS [10] after each iteration. The missing roof is reconstructed gradually, and good result is finally achieved in Fig. 15 (6).

Fig. 16 shows the intermediate results during the fast 3D modeling. To demonstrate the importance of multiview fusion, we show the results without and with multiple view fusion at the first and second rows respectively. Fig. 16 (a) shows a color coded confidence map at a sample input image, where red means less confident. (b) shows the triangle depth map, and (c) shows the fusion of all depth maps.

2) *Running Time*: In Table I, we report our system's running time on the 1st iteration of the example *Church*. Note the our MVS takes 14.7 second for 64 images, including the over-segmentation and Delaunay triangulation. We used the Poisson surface reconstruction from [38], which takes 20 seconds to return a complete surface. In total, our system takes 34.7 seconds to generate a surface mesh from these 64 images. In comparison, the MVE [15] and CMP-MVS [10] systems take about 30 minutes and 40 minutes to reconstruct a mesh, though at high quality. The NBV selection takes another 6.1 second, and the path planning is less than 0.01 second.

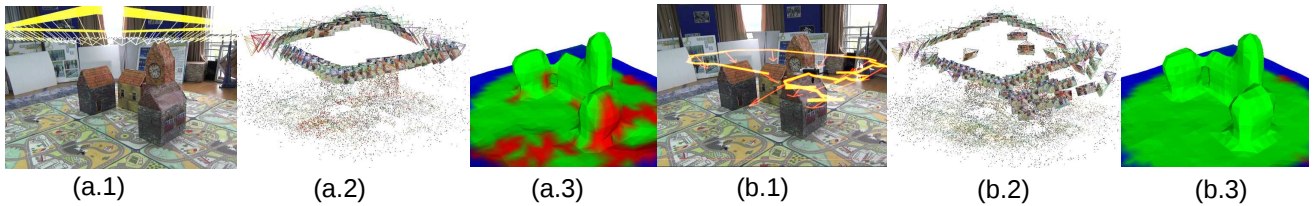


Fig. 17: The *Indoor* example with a Bebop drone in a Vicom room.

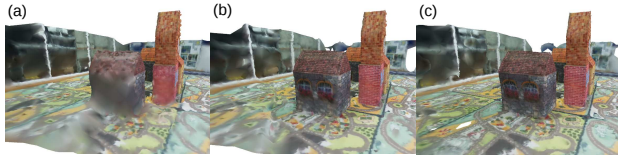


Fig. 18: CMP-MVS results after each iteration.

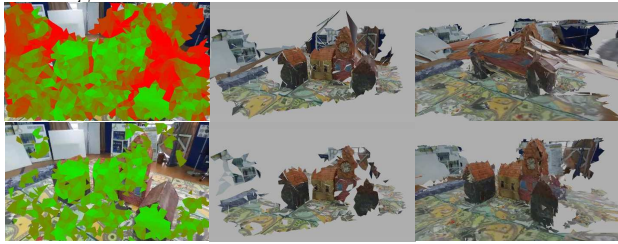


Fig. 19: Triangle depth map estimation on the *Indoor* example. The first and second rows are results before and after multiview fusion. From left to right, they are: (a) confidence measure of the depth map, where red means low confidence; (b) sample depth map from a single view. (c) fused depth map from all views.

## B. Indoor Experiments

We further verify our system in a Vicom room decorated with some cardboard boxes resembling buildings. The UAV's pose is captured by Vicom for real-time control. The UAV transmits low-res ( $640 \times 368$ ) images in real-time to the ground station while keeps high-res ( $1920 \times 1080$ ) images on board for offline process. 64 images are captured from the initial scan. This model is covered in 3 iterations. Fig. 17 shows the result at the first and last iteration. Again, (a.1) and (b.1) are the flight paths and view orientations, (a.2) and (b.2) are SfM results. (a.3) and (b.3) are the coverage evaluation result. The 3D models generated by CMP-MVS [10] are shown in Fig. 18. From the left of Fig. 17, we can tell the 3D model quality is well predicted by the coverage map in Fig. 17 (a.3). Our NBVs successfully identify a small set of images to improve the model, which is verified by both the coverage map in Fig. 17 (b.3) and the good model at the right of Fig. 18.

Fig. 19 shows a comparison of triangle depth map with and without multiview fusion. It is clear that the fusion strategy significantly improves the 3D reconstruction.

## C. Outdoor Experiments

We further demonstrate our system with real examples in outdoor open areas.

1) *Asian Building*: Fig. 1 shows the building that is a 15-meter high entrance gate. We initialize image capture with a rectangular flight path at 18 meter high (see the reconstructed

camera trajectory in Fig. 1 (a.1)). This model is well reconstructed after 4 iterations of image capturing. Fig. 1 (a.2) and (b.2) show the color coded coverage result and some selected NBVs. In the initialization, some part under the roof is not covered by the input images, as indicated in red in Fig. 1 (a.2). Our system will guide the UAV to gradually lower down and raise its camera pitch angle to capture those regions. This process can be seen from the visualized NBVs in Fig. 1 (b.2), where NBVs at different iterations are shown in different color. After additional images are taken, the coverage map in Fig. 1 (b.2) turns to green. Fig. 1 (b.3) shows the high quality 3D models produced by the offline modeling system with all images.

2) *Eagle*: The *Eagle* example is a 10-meter statue as shown in Fig. 13. The initial viewpoints are sampled every 2 meters along a rectangular path that is 10 meters above the ground. The initial camera pitch angle is 30 degrees downward. The model is covered in 8 iterations of image capture. During these iterations, the drone automatically lowers its height and raises camera's pitch angle to capture the missing regions under the eagle's wings. For example, at the second iteration, the drone raises its pitch angle to 15 degree downwards. At the fourth iteration, since the major uncovered region is at the base of the statue, the drone change its pitch angle back to 30 degrees downward again. To keep the view overlap with previously captured images, the drone only reduces its height for less than 2 meters between two iterations. The CMP-MVS results after iteration 1, 4 and 8 are shown in Fig. 14. Note that the region under the wings and the lower base are improved.

## VI. CONCLUSION

This paper presents a method to automate the image-capturing process in large scale image-based modeling. Technically, it contributes a novel and efficient multi-view stereo (MVS) algorithm and an efficient next-best-view (NBV) algorithm. The MVS algorithm computes a 3D triangle mesh at each input image and fuses the results from different images together. The whole problem is solved by an iterative linear method, which makes online model reconstruction and assessment possible. The NBV algorithm is tailored for the image-based modeling application. It ensures the UAV is always flying above unknown shapes to avoid possible collisions. Putting these together, we present an online active image-based modeling system, that can automatically reconstruct a 3D model, assess its quality, and capture additional data to improve the model.



## REFERENCES

- [1] Noah Snavely, Steven M Seitz, and Richard Szeliski. Photo tourism: exploring photo collections in 3d. In *ACM Trans. on Graphics*, volume 25, pages 835–846. ACM, 2006.
- [2] Sameer Agarwal, Noah Snavely, Ian Simon, Steven M Seitz, and Richard Szeliski. Building rome in a day. In *Proc. IEEE Int. Conf. on Computer Vision*, 2009.
- [3] Changchang Wu. Towards linear-time incremental structure from motion. In *Int. Conf. on 3D Vision*, pages 127–134. IEEE, 2013.
- [4] Michael Goesele, Noah Snavely, Brian Curless, Hugues Hoppe, and Steven M Seitz. Multi-view stereo for community photo collections. In *Proc. IEEE Int. Conf. on Computer Vision*. IEEE, 2007.
- [5] Simon Fuhrmann and Michael Goesele. Floating scale surface reconstruction. *Proc. of ACM SIGGRAPH*, 33(4): 46, 2014.
- [6] Robert Bridson. Fast poisson disk sampling in arbitrary dimensions. In *Proc. of ACM SIGGRAPH*, page 22, 2007.
- [7] Ping Tan, Gang Zeng, Jingdong Wang, Sing Bing Kang, and Long Quan. Image-based tree modeling. In *Proc. of ACM SIGGRAPH*, volume 26. ACM, 2007.
- [8] Jianxiong Xiao, Tian Fang, Ping Tan, Peng Zhao, Eyal Ofek, and Long Quan. Image based facade modeling. *ACM Trans. on Graphics*, 27, 2009.
- [9] Pascal Muller, Gang Zeng, Peter Wonka, and Luc Van Gool. Image based procedural modeling of facades. *ACM Trans. on Graphics*, 26, 2007.
- [10] Michal Jancosek and Tomáš Pajdla. Multi-view reconstruction preserving weakly-supported surfaces. In *Proc. IEEE Conf. on Computer Vision & Pattern Recognition*, pages 3121–3128. IEEE, 2011.
- [11] Simon Fuhrmann, Fabian Langguth, and Michael Goesele. Mve-a multi-view reconstruction environment. In *EUROGRAPHICS Workshops on Graphics and Cultural Heritage*, pages 11–18, 2014.
- [12] <https://www.altizure.com>.
- [13] <https://pix4d.com/>.
- [14] George Vogiatzis, Carlos Hernández Esteban, Philip HS Torr, and Roberto Cipolla. Multiview stereo via volumetric graph-cuts and occlusion robust photo-consistency. *IEEE Trans. on Pattern Analysis & Machine Intelligence*, 29(12):2241–2246, 2007.
- [15] Michael Goesele, Brian Curless, and Steven M Seitz. Multi-view stereo revisited. In *Proc. IEEE Conf. on Computer Vision & Pattern Recognition*, volume 2, pages 2402–2409. IEEE, 2006.
- [16] Olivier Faugeras and Renaud Keriven. Complete dense stereovision using level set methods. In *Euro. Conf. on Computer Vision*, pages 379–393, 1998.
- [17] Yasutaka Furukawa, Brian Curless, Steven M Seitz, and Richard Szeliski. Towards internet-scale multi-view stereo. In *Proc. IEEE Conf. on Computer Vision & Pattern Recognition*. IEEE, 2010.
- [18] Maxime Lhuillier and Long Quan. A quasi-dense approach to surface reconstruction from uncalibrated images. *IEEE Trans. on Pattern Analysis & Machine Intelligence*, 27(3):418–433, 2005.
- [19] András Bódis-Szomorú, Hayko Riemenschneider, and Luc Van Gool. Superpixel meshes for fast edge-preserving surface reconstruction. In *Proc. IEEE Conf. on Computer Vision & Pattern Recognition*, pages 2011–2020, 2015.
- [20] Cl Connolly. The determination of next best views. In *Proc. IEEE Int. Conf. Robotics and Automation*, volume 2, pages 432–435. IEEE, 1985.
- [21] Shengyong Chen, Youfu Li, and Ngai Ming Kwok. Active vision in robotic systems: A survey of recent developments. *Int. J. of Robotics Research*, 30(11):1343–1377, 2011.
- [22] Simon Kriegel, Christian Rink, Tim Bodenmüller, and Michael Suppa. Efficient next-best-scan planning for autonomous 3d surface reconstruction of unknown objects. *J. of Real-Time Img. Proc.*, 10(4):611–631, 2015.
- [23] Souhaïel Khalfaooui, Ralph Seulin, Yohan Fougerolle, and David Fofi. An efficient method for fully automatic 3d digitization of unknown objects. *Computers in Industry*, 64(9):1152–1160, 2013.
- [24] Matteo Dellepiane, Emanuele Cavarretta, Paolo Cignoni, and Roberto Scopigno. Assisted multi-view stereo reconstruction. In *Int. Conf. on 3D Vision*, pages 318–325. IEEE, 2013.
- [25] Shihao Wu, Wei Sun, Pinxin Long, Hui Huang, Daniel Cohen-Or, Minglun Gong, Oliver Deussen, and Baoquan Chen. Quality-driven poisson-guided autoscanning. *ACM Trans. on Graphics*, 33(6), 2014.
- [26] Enrique Dunn and Jan-Michael Frahm. Next best view planning for active model improvement. In *Proc. British Machine Vision Conf.*, pages 1–11, 2009.
- [27] Michael Trummer, Christoph Munkelt, and Joachim Denzler. Online next-best-view planning for accuracy optimization using an extended e-criterion. In *Int. Conf. on Pattern Recognition*, pages 1642–1645. IEEE, 2010.
- [28] Christof Hoppe, Manfred Klopschitz, Markus Rumpler, Andreas Wendel, Stefan Kluckner, Horst Bischof, and Gerhard Reitmayr. Online feedback for structure-from-motion image acquisition. In *Proc. British Machine Vision Conf.*, volume 2, 2012.
- [29] Christof Hoppe, Andreas Wendel, Stefanie Zollmann, Katrin Pirker, Arnold Irschara, Horst Bischof, and Stefan Kluckner. Photogrammetric camera network design for micro aerial vehicles. In *Computer vision winter workshop*, volume 8, 2012.
- [30] Christian Mostegel, Markus Rumpler, Friedrich Fraundorfer, and Horst Bischof. Uav-based autonomous image acquisition with multi-view stereo quality assurance by confidence prediction. In *Proc. IEEE Conf. on Computer Vision & Pattern Recognition Workshops*, 2016.
- [31] Changchang Wu et al. Visualsfm: A visual structure from motion system. 2011.

- [32] Liuyun Duan and Florent Lafarge. Image partitioning into convex polygons. In *Proc. IEEE Conf. on Computer Vision & Pattern Recognition*, pages 3119–3127, 2015.
- [33] Steven Fortune. Voronoi diagrams and delaunay triangulations. *Computing in Euclidean geometry*, 1(193-233): 2, 1992.
- [34] Michael Kazhdan and Hugues Hoppe. Screened poisson surface reconstruction. *ACM Trans. on Graphics*, 32(3): 29, 2013.
- [35] Gino van den Bergen. Efficient collision detection of complex deformable models using aabb trees. *J. of Graphics Tools*, 2(4):1–13, 1997.
- [36] <https://http://www.gazebosim.org/>.
- [37] <https://3dwarehouse.sketchup.com/?hl=en>.
- [38] <http://www.cs.jhu.edu/~misha/code/poissonrecon/version5.5/>.